

Constant-power versus constant-voltage actuation in frequency sweeps for acoustofluidic applications

Fabian Lickert,^{*} Henrik Bruus,[†] and Massimiliano Rossi[‡]
*Department of Physics, Technical University of Denmark,
DTU Physics Building 309, DK-2800 Kongens Lyngby, Denmark*
(Dated: 4 October 2022)

Supplying a piezoelectric transducer with constant voltage or constant power during a frequency sweep can lead to different results in the determination of the acoustofluidic resonance frequencies, which are observed when studying the acoustophoretic displacements and velocities of particles suspended in a liquid-filled microchannel. In this work, three cases are considered: (1) Constant input voltage into the power amplifier, (2) constant voltage across the piezoelectric transducer, and (3) constant average power dissipation in the transducer. For each case, the measured and the simulated responses are compared, and good agreement is obtained. It is shown that Case 1, the simplest and most frequently used approach, is largely affected by the impedance of the used amplifier and wiring, so it is therefore not suitable for a reproducible characterization of the intrinsic properties of the acoustofluidic device. Case 2 strongly favors resonances at frequencies yielding the lowest impedance of the piezoelectric transducer, so small details in the acoustic response at frequencies far from the transducer resonance can easily be missed. Case 3 provides the most reliable approach, revealing both the resonant frequency, where the power-efficiency is the highest, as well as other secondary resonances across the spectrum.

Keywords: acoustofluidics, microparticle acoustophoresis, general defocusing particle tracking, particle-velocity spectroscopy.

1. INTRODUCTION

In many experimental acoustofluidic platforms, the device is actuated by an attached piezoelectric transducer, driven by a sine-wave generator through a power amplifier. To describe the performance of the acoustofluidic actuation, the operating conditions are typically expressed in terms of the voltage amplitude or the electric power dissipation together with quantities such as the acoustic energy density, the acoustic focusing time, or achievable flow rates [1–3]. Often, it is however left unclear under which conditions and at which point in the electric circuit, the relevant quantities such as voltage amplitude or power dissipation have been measured. Recent studies compare device performance at constant average power for different placements of the transducer [4, 5]. Dubay *et al.* [6] performed thorough power and voltage measurements for the evaluation of their acoustofluidic device, however, they noted that the actual power delivered to the transducer might reduce to only a fraction (as low as 10%) of the reported value. The likely cause of this reduction is that the transducer is acting as a large capacitive load, where electrical impedance matching between source and load impedance is difficult to accomplish [6, 7].

Whereas optimization of the driving circuit is customary in other fields, such as ultrasonic transducers for cellular applications [8], non-destructive testing [9], and pulse-echo systems [10], this has not been given much consideration in the field of acoustofluidics, where the focus often lies on optimizing the acoustic impedance matching [11, 12], while neglecting the impact of the driving circuit. A recent work, though, considers topics such as electrical impedance matching in the context of developing low-cost and possibly hand-held driving circuits for acoustofluidics [13]. To our knowledge, studies have not yet been performed, in which the impact of different electrical excitation methods on

^{*} fabianl@dtu.dk

[†] bruus@fysik.dtu.dk

[‡] rossi@fysik.dtu.dk

a transducer in a given acoustofluidic device is compared with respect to the resulting acoustophoretic particle focusing.

In the case of bulk piezoelectric transducers, where the electrical impedance ranges over several orders of magnitude as a function of frequency, the voltage amplitude across the transducer can differ severely from the amplitude expected by simply considering the voltage input at the amplifier. Suitable voltage compensation circuits or voltage correction methods should be used to achieve the desired voltage amplitude directly at the transducer. Furthermore, a standard has not yet been established whether it is more beneficial to run frequency sweeps at a constant voltage or at a constant power. We therefore in this work investigate the impact of three different actuation approaches during a frequency sweep: (1) Constant input voltage into the amplifier, (2) constant voltage at the transducer, and (3) constant power dissipation in the transducer. We compare experimental findings with our numerical model. The aim of this paper is to establish guidelines on which actuation approach is preferable for acoustofluidic applications using bulk piezoelectric transducers to generate acoustophoresis in bulk acoustic waves.

The paper is structured in the following way: In Section 2 a brief summary is given of the governing equations for the pressure field, the displacement field, and the electric potential in our acoustofluidic device. Section 3 gives an overview of our experimental setup, and the procedure used for the measurement of the particle velocities is described step by step. In Section 4 we describe the numerical approach used in our study, and in Section 5 we compare several aspects of the obtained results for the device under study: a comparison between the electrical characteristics of the device, as well as the numerically and experimentally observed acoustophoretic particle velocities are given. Furthermore, some details of the simulated fields are shown. Finally, the paper concludes in Section 6 with a short summary and some guidelines on the actuation of piezoelectric transducers for acoustofluidic applications.

2. THEORY

The theoretical approach follows our previous work [3, 14–16], in which the computational effort in the simulations are reduced by employing the effective-boundary-layer theory derived by Bach and Bruus [17]. We assume time-harmonic first-order fields with angular frequency $\omega = 2\pi f$ for the acoustic pressure $\tilde{p}_1(\mathbf{r}, t) = p_1(\mathbf{r}) e^{-i\omega t}$, the electric potential $\tilde{\varphi}(\mathbf{r}, t) = \varphi(\mathbf{r}) e^{-i\omega t}$, and the displacement field $\tilde{\mathbf{u}}(\mathbf{r}, t) = \mathbf{u}(\mathbf{r}) e^{-i\omega t}$. Derived through a perturbation approach, these fields represent tiny perturbations of the unperturbed zero-order fields.

2.1. Governing equations

For a fluid with speed of sound c_0 , density ρ_0 , dynamic and bulk viscosity of the fluid η_0 and η_0^b , damping coefficient Γ_0 , and the isentropic compressibility $\kappa_0 = (\rho_0 c_0^2)^{-1}$, the acoustic pressure p_1 is governed by the Helmholtz equation, and the acoustic velocity \mathbf{v}_1 is a gradient field,

$$\nabla^2 p_1 = -\frac{\omega^2}{c_0^2} (1 + i\Gamma_0) p_1, \text{ with } \Gamma_0 = \left(\frac{4}{3}\eta_0 + \eta_0^b\right) \omega \kappa_0, \quad (1a)$$

$$\mathbf{v}_1 = -i \frac{1 - i\Gamma_0}{\omega \rho_0} \nabla p_1 \quad (1b)$$

For an elastic solid with density ρ_{sl} , the displacement field \mathbf{u} is governed by the Cauchy equation

$$-\omega^2 \rho_{sl} \mathbf{u} = \nabla \cdot \boldsymbol{\sigma}, \quad (2)$$

where $\boldsymbol{\sigma}$ is the stress tensor. In the Voigt notation, the 1×6 stress $\boldsymbol{\sigma}$ and strain \mathbf{s} column vectors are given by the 6×1 transposed row vectors $\boldsymbol{\sigma}^T = (\sigma_{xx}, \sigma_{yy}, \sigma_{zz}, \sigma_{yz}, \sigma_{xz}, \sigma_{xy})$

and $\mathbf{s}^\top = (\partial_x u_x, \partial_y u_y, \partial_z u_z, \partial_y u_z + \partial_z u_y, \partial_x u_z + \partial_z u_x, \partial_x u_y + \partial_y u_x)$, respectively, and $\boldsymbol{\sigma}$ is related to \mathbf{s} by the 6×6 stiffness tensor \mathbf{C} having the elastic moduli C_{ik} as components. For a linear, isotropic, elastic solid of the ∞mm -symmetry class the relation is,

$$\boldsymbol{\sigma} = \mathbf{C} \cdot \mathbf{s}, \quad \mathbf{C} = \begin{pmatrix} C_{11} & C_{12} & C_{13} & 0 & 0 & 0 \\ C_{12} & C_{11} & C_{13} & 0 & 0 & 0 \\ C_{13} & C_{13} & C_{33} & 0 & 0 & 0 \\ 0 & 0 & 0 & C_{44} & 0 & 0 \\ 0 & 0 & 0 & 0 & C_{44} & 0 \\ 0 & 0 & 0 & 0 & 0 & C_{66} \end{pmatrix}. \quad (3)$$

Here, the components $C_{ik} = C'_{ik} + iC''_{ik}$ are complex-valued with real and imaginary parts relating to the speed and the attenuation of sound waves in the solid, respectively. In this work we assume the glass and the glue layer to be isotropic, yielding the following relations $C_{33} = C_{11}$, $C_{66} = C_{44}$ and $C_{13} = C_{12} = C_{11} - 2C_{44}$. This leaves the two independent complex-valued parameters C_{11} and C_{44} , relating to the longitudinal and transverse speed of sound and attenuation in the glass and glue layer. For a lead zirconate titanate (PZT) transducer, $C_{66} = \frac{1}{2}(C_{11} - C_{12})$, which leaves five independent complex-valued elastic moduli, C_{11} , C_{12} , C_{13} , C_{33} , and C_{44} .

The electrical potential φ inside the PZT transducer is governed by Gauss's law for a linear, homogeneous dielectric with a zero density of free charges,

$$\nabla \cdot \mathbf{D} = \nabla \cdot (-\boldsymbol{\varepsilon} \cdot \nabla \varphi) = 0, \quad (4)$$

where \mathbf{D} is the electric displacement field and $\boldsymbol{\varepsilon}$ the dielectric tensor. Furthermore in PZT, the complete linear electromechanical coupling relating the stress and the electric displacement to the strain and the electric field is given as,

$$\begin{pmatrix} \boldsymbol{\sigma} \\ \mathbf{D} \end{pmatrix} = \begin{pmatrix} \mathbf{C} & -\mathbf{e}^\top \\ \mathbf{e} & \boldsymbol{\varepsilon} \end{pmatrix} \begin{pmatrix} \mathbf{s} \\ \mathbf{E} \end{pmatrix}, \quad (5a)$$

$$\text{with } \mathbf{e} = \begin{pmatrix} 0 & 0 & 0 & 0 & e_{15} & 0 \\ 0 & 0 & 0 & e_{15} & 0 & 0 \\ e_{31} & e_{31} & e_{33} & 0 & 0 & 0 \end{pmatrix} \text{ and } \boldsymbol{\varepsilon} = \begin{pmatrix} \varepsilon_{11} & 0 & 0 \\ 0 & \varepsilon_{11} & 0 \\ 0 & 0 & \varepsilon_{33} \end{pmatrix}. \quad (5b)$$

2.2. The acoustic radiation force and the acoustophoretic particle velocity

We consider polystyrene particles with density ρ_{ps} , compressibility κ_{ps} , and a radius a , which is much larger than the viscous boundary layer and much smaller than the acoustic wavelength. In this case, the acoustic radiation force \mathbf{F}^{rad} on the particles placed in water is given by the negative gradient of the Gorkov potential U^{rad} , [18]

$$\mathbf{F}^{\text{rad}} = -\nabla U^{\text{rad}}, \quad \text{with} \quad (6a)$$

$$U^{\text{rad}} = \pi a^3 \left(\frac{1}{3} f_0 \kappa_0 |p_1|^2 - \frac{1}{2} f_1 \rho_0 |\mathbf{v}_1|^2 \right), \quad f_0 = 1 - \frac{\kappa_{\text{ps}}}{\kappa_0}, \quad \text{and} \quad f_1 = \frac{2(\rho_{\text{ps}} - \rho_0)}{2\rho_{\text{ps}} + \rho_0}. \quad (6b)$$

If a (polystyrene) microparticle of radius a is placed in a fluid of viscosity η_0 flowing with the local velocity \mathbf{v}_0 , the presence of \mathbf{F}^{rad} imparts a so-called acoustophoretic velocity \mathbf{v}_{ps} to the particle. As inertia is negligible, \mathbf{v}_{ps} is found from a balance between \mathbf{F}^{rad} and the viscous Stokes drag force \mathbf{F}^{drag} , [14]

$$\mathbf{v}_{\text{ps}} = \frac{1}{6\pi\eta_0 a} \mathbf{F}^{\text{rad}} + \mathbf{v}_0. \quad (7)$$

2.3. Electrical impedance and power dissipation

For a PZT transducer with an excited top electrode and a grounded bottom electrode set by the respective potentials $\varphi = \varphi_{\text{pzt}}$ and $\varphi = 0$ V, the electrical impedance Z is given by the ratio of $\varphi_{\text{pzt}} - 0$ V and the surface integral of the polarization current density $\mathbf{D} + \epsilon_0 \nabla \varphi$ as, [15]

$$Z = \frac{\varphi_{\text{pzt}}}{I}, \quad \text{with } I = -i\omega \int_{\partial\Omega} \mathbf{n} \cdot (\mathbf{D} + \epsilon_0 \nabla \varphi) da. \quad (8)$$

The electrical power dissipation P_{pzt} in the PZT transducer is given by

$$P_{\text{pzt}} = \frac{1}{2} \text{Re} [(\varphi_{\text{pzt}})I^*] = \frac{1}{2} |\varphi_{\text{pzt}}| |I| \cos \theta, \quad \text{with } \theta = \arg(Z). \quad (9)$$

2.4. Butterworth–Van Dyke circuit model

To describe the electrical response of the transducer around its thickness resonance frequency, we use a single-frequency Butterworth-Van Dyke (BVD) model. We furthermore include the impact of the wiring and the parasitic effects of the circuit leading to the PZT transducer in our model. An equivalent circuit of our model is shown in Fig. 1(a). It consists of the parasitic wire resistance R_{wire} and inductance L_{wire} in series with a PZT circuit having the transducer capacitance C_0 in parallel with an transducer LCR-circuit R_1 - L_1 - C_1 . The four parameters R_1 , L_1 , C_1 , and C_0 can be obtained from the PZT admittance spectrum $Y(f) = 1/Z(f)$ at the resonance frequency f_r and anti-resonance frequency f_a [19, 20],

$$C_0 = \frac{\text{Im} Y(f_r)}{2\pi f_r}, \quad R_1 = \frac{1}{\text{Im} Y(f_r)}, \quad C_1 = C_0 \left[\frac{f_a^2}{f_r^2} - 1 \right], \quad L_1 = \frac{1}{(2\pi f_r)^2 C_1}. \quad (10)$$

We perform simulations of the BVD-circuit using the *SPICE*-based circuit simulator software *LTspice* with parameters for the circuit components obtained via Eq. (10) and the measured values of the wire resistance R_{wire} and inductance L_{wire} .

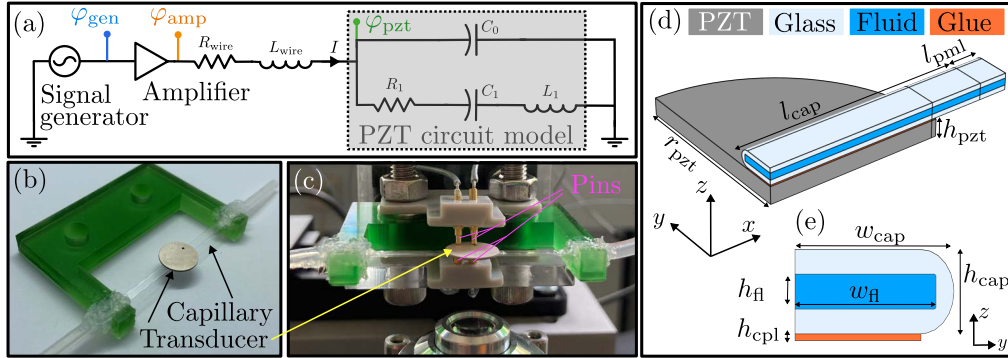


FIG. 1. (a) A schematic overview of the electrical circuit driving the transducer. The transducer, represented by the BVD-model with a resistor R_1 , an inductor L_1 , and two capacitors C_0 and C_1 , is coupled in series with the parasitic wire resistance and inductance. (b) A disk-shaped piezoelectric transducer is glued to a long, straight glass capillary tube. The tube is connected to a 3D-printed sample holder (green), and inlet/outlet tubing is glued to the ends of the tube. (c) The acoustofluidic device is mounted above the microscope lens and iselectrically connected via two spring-loaded pins on each side of the transducer. (d) Using the symmetry planes x - z and y - z , only a quarter of the actual geometry needs to be simulated numerically. The different domains of the model: PZT (gray), glass (light blue), water (dark-blue), and the thin glue layer (orange). The dimensions are $r_{\text{pzt}} = 5.02$ mm, $h_{\text{pzt}} = 506$ μm , $w_{\text{fl}} = 2060$ μm , $h_{\text{fl}} = 200$ μm , $h_{\text{cpl}} = 39$ μm , $w_{\text{cap}} = 2324$ μm , and $h_{\text{cap}} = 483$ μm . In the simulation the reduced lengths are $l_{\text{cap}} = 6.44$ mm and $l_{\text{pml}} = 839$ μm . (e) The cross-section in the y - z -plane showing the glass tube, the water, and the glue layer.

3. MATERIALS AND METHODS

3.1. The experimental setup

In this work, an acoustofluidic device is used, that consists of a 483- μm -thick, 2324- μm -wide and 50.9-mm-long glass capillary (VitroTubes, VitroCOM, Mountain Lakes, USA) containing a 200 μm high and 2.06 mm wide microchannel. The device is glued to a cylindrical piezoelectric transducer disk (Pz27, Meggitt A/S, Kvistgaard, Denmark), made from PZT, of thickness 506 μm and diameter 10.045 mm with a nominal resonance frequency at around 4 MHz. The capillary tube is glued to the transducer by a thin (39 μm) layer of UV-curable glue (NOA 86H, Norland Products, Jamesburg, USA). An overview of the device is shown in Fig. 1(b). Using silicone glue, the device is mounted on a 3D-printed sample holder, and rubber tubing is glued to the glass capillary tube on both ends. The electrical connection to the piezoelectric transducer is made via four spring-loaded pins, as can be seen in Fig. 1(c). These pins both minimize the clamping force on the transducer and enables four-probe measurement of the electric voltage across the transducer.

A schematic overview of the electrical circuit, including signal generator and amplifier is shown in Fig. 1(a). As signal generator an Analog Discovery 2 (Digilent, Pullman, USA) in connection with the power amplifier TOE 7607 (TOELLNER Electronic Instrumente GmbH, Herdecke, Germany) was used to drive the piezoelectric transducer. The output of the amplifier is connected to the spring-loaded pins via a coaxial cable followed by 30 cm hookup wire. The wire is considered as a short transmission line with negligible capacitance, but with non-negligible parasitic resistance R_{wire} and inductance L_{wire} . In our simplified circuit model, we only consider the thickness resonance at around 4 MHz of the transducer, and model the transducer via the BVD-model of Eq. (10).

3.2. Fabrication and characterization of the devices

The device is assembled in a step-by-step procedure, and after each fabrication step the electrical impedance spectrum $Z(f)$ of the piezoelectric transducer is recorded with the Vector Network Analyzer Bode 100 (OMICRON electronics GmbH, Klaus, Austria) in the range from 500 Hz to 5 MHz. Device dimensions were measured using an electronic micrometer (RS Pro, RS Components, Corby, UK) with an accuracy of $\pm 4 \mu\text{m}$. The assembly process consisted of the followings seven steps:

1. Measure the dimensions of the capillary tube and the transducer.
2. Measure the initial impedance spectrum $Z_{\text{init}}(f)$ of the Pz27 disk.
3. Fit the Pz27 material parameters using ultrasound electrical impedance spectroscopy (UEIS), following the method described in Ref. [21].
4. Glue the capillary tube onto the transducer and UV-curing using an exposure time of 168 s at a UV-intensity of 15 mW/cm^2 and a wavelength of 365 nm.
5. Measure the total device thickness to obtain the glue layer thickness.
6. Mount the device on a 3D-printed sample holder and connection to rubber tubing using silicone glue.
7. Measure the impedance spectrum $Z_{\text{sys}}(f)$ of the combined capillary-glue-transducer system, both air- and fluid-filled.

Using the four-probe setup, shown in Fig. 1(a),(c), the voltage amplitudes φ_{gen} at the signal generator, φ_{amp} at the amplifier, and φ_{pzt} directly across at the transducer were recorded during the measurements. The time-averaged dissipated power P_{pzt} for a given frequency f was calculated from Eq. (9) as

$$P_{\text{pzt}}(f) = \frac{1}{2} \frac{\varphi_{\text{pzt}}^2 \cos[\theta_{\text{sys}}(f)]}{|Z_{\text{sys}}(f)|}, \quad \text{with } \theta_{\text{sys}} = \arg(Z_{\text{sys}}). \quad (11)$$

A feedback control system was implemented to actuate the transducer at the desired constant power or constant voltage during the frequency sweeps. In the following analysis, we consider the following three case:

- (**Case 1**): Constant voltage at the generator, $\varphi_{\text{gen}} = 1$ V.
 (**Case 2**): Constant voltage at the transducer, $\varphi_{\text{pzt}} = 0.5$ V.
 (**Case 3**): Constant power dissipation in the transducer, $P_{\text{pzt}} = 50$ mW.

3.3. Determination of acoustofluidic resonance frequencies by particle tracking velocimetry

The acoustofluidic resonance frequencies were determined by measuring the average velocity of particles focusing under acoustofluidic actuation. For the particle focusing experiment, we used a neutrally buoyant solution of 10- μm -diameter fluorescent polystyrene spheres (microparticles GmbH, Berlin, Germany) in a fluid consisting of 83% (v/v) of ultrapure water (Direct-Q3 System, Merck) and 17% (v/v) OptiPrep (Density Gradient Medium, Sigma-Aldrich). The particle concentration was about 500 particles/ μL .

The acoustic focusing was studied using single-camera 3D particle tracking performed with the general defocusing particle tracking (GDPT) method [22]. GDPT determines the depth position of defocused particle images from the analysis of the corresponding defocusing patterns, previously mapped with a proper calibration procedure [23]. The particle images were recorded using a high-sensitive sCMOS camera (pco.edge 5.5, Excelitas PCO GmbH, Kelheim, Germany) with an optical system consisting of a $5\times$ microscope objective (EC EPIPlan, Zeiss AG, Oberkochen, Germany) and a cylindrical lens in front of the camera sensor to enhance the defocusing patterns. The images were processed using the open-source software *defocustracker* version 2.0.0 [24].

In each experiment, 200 images were recorded at 25 frames/s, and the signal generator was switched on precisely 1 s after the camera had started to record the first frame using an electrical trigger. The frequency sweeps were performed at frequencies in the range from 3.3 to 4.3 MHz in steps of 10 kHz. After the GDPT evaluation, we obtained a set of N measured three-dimensional particle trajectories $\mathbf{s}^{(j)}(t) = \{x(t), y(t), z(t)\}^{(j)}$ for each frequency. We then proceed to compute the three components $s_i^{\text{exp}}(t)$ of the average cumulative particle displacement vector $\mathbf{s}^{\text{exp}}(t)$ as

$$s_i^{\text{exp}}(t) = \frac{1}{N} \sum_{j=1}^N |s_i^{(j)}(t) - s_i^{(j)}(t_0)|, \quad \text{for } i = x, y, z, \quad (12)$$

where t_0 is the time when the acoustics are turned on. The average acoustophoretic speed v_{exp} of the particles is then calculated at time $t_{\text{exp}} = 40$ ms after turning on the acoustics, as

$$v_{\text{exp}} = \sqrt{\sum_{i=x,y,z} \left(\partial_t s_i^{\text{exp}}|_{t=t_{\text{exp}}} \right)^2}. \quad (13)$$

4. NUMERICAL MODEL

4.1. Description of the modeled system

We perform numerical simulations of the device described in Section 3.3.1 using the software COMSOL Multiphysics 6.0, following the implementation in Ref. [3, 14, 25]. By using the x - z and y - z symmetry planes, only a quarter of the actual geometry is modeled. In the model we consider the piezoelectric transducer, a thin coupling layer, and the water-filled glass capillary tube. To further minimize the computational complexity, we apply a perfectly matched layer (PML) at the end of the glass capillary [25]. The PML mimicks perfect absorption of all outgoing waves, and it allows to reduce the length of the capillary tube. In our experimental setup, the damping at the edge of the tube is ensured by the silicone glue connecting the tube to the sample holder. A sketch of the system is shown in Fig. 1(d,e). Simulations were performed on a workstation with a 12-core, 3.5-GHz central processing unit and 128 GB random access memory. Details on the mesh convergence analysis and the material parameters used for the simulation can be found in Appendix A and B.

4.2. Numerical simulation of the particle velocity

In our simulation model, we use the "Particle Tracing for Fluid Flow" module and compute the particle trajectories of 1000 randomly distributed particles. The wall condition is set to "Stick" to mimic stuck particles, which were also commonly observed in the experimental setup. The force acting on the particles is the simulated radiation force \mathbf{F}^{rad} , see Eq. (6). Acoustic streaming is neglected due to the size of the particles, and the influence of gravity is neglected due to the use of a neutrally-buoyant solution. Similarly to what is done for the experimental data, we obtain the velocity \mathbf{v}_i of each particle i at time t_{sim} and compute the average speed v_{sim} of the particle as

$$v_{\text{sim}} = \frac{1}{N} \sum_{i=1}^N |\mathbf{v}_i(t_{\text{sim}})|, \quad (14)$$

at time $t_{\text{sim}} = (40 t_{\text{foc}}^{\text{sim}}/t_{\text{foc}}^{\text{exp}})$ ms, where $t_{\text{foc}}^{\text{sim}}/t_{\text{foc}}^{\text{exp}}$ is the ratio between the numerical and experimental focusing time at resonance.

4.3. Boundary conditions between liquid, solid, and PZT

In the simulations, we assume a time-harmonic voltage amplitude of φ_{pzt} at the top surface of the piezoelectric transducer, while the bottom surface is grounded to $\varphi_{\text{gnd}} = 0$. We furthermore assume continuous stress between the different domains, a normal component of the dielectric displacement field $\mathbf{D} \cdot \mathbf{n} = 0$ at interface PZT–air and zero normal stress at the outer surfaces of the solid domains [14]. For the interface between solid and fluid, we implement the effective boundary conditions derived by Bach and Bruus [17]. Here, the fields inside the very thin boundary layers of thickness $\delta_{\text{fl}} = \sqrt{2\eta_0/(\rho_0\omega)} \approx 0.5 \mu\text{m}$ are taken into account analytically. The pressure p_1 at the fluid–air interface is set to zero. The boundary conditions between the different domains and their corresponding boundary are summarized in Table 1.

We assume symmetry of all simulated fields at the yz -plane at $x = 0$ and at the xz -plane at $y = 0$. The symmetry boundary conditions therefore are implemented as follows:

Symmetry at $x = 0$:

$$u_x = 0, \quad \sigma_{yx} = \sigma_{zx} = 0, \quad \partial_x p_1 = 0, \quad \partial_x \varphi = 0. \quad (15a)$$

Symmetry at $y = 0$:

$$u_y = 0, \quad \sigma_{xy} = \sigma_{zy} = 0, \quad \partial_y p_1 = 0, \quad \partial_y \varphi = 0. \quad (15b)$$

TABLE 1. The boundary conditions used in the numerical simulations with the surface normal vector \mathbf{n} pointing away from the respective domain. We use the solid velocity $\mathbf{v}_{\text{sl}} = -i\omega\mathbf{u}$, and the complex-valued shear-wave number $k_s = (1+i)\delta_{\text{fl}}^{-1} = (1+i)\sqrt{\rho_0\omega/(2\eta_0)}$.

Domain	← Boundary	Boundary condition
PZT	← top electrode	$\varphi = \varphi_{\text{pzt}}$
PZT	← bottom electrode	$\varphi = 0$
PZT	← air	$\mathbf{D} \cdot \mathbf{n} = 0$
Solid	← air	$\boldsymbol{\sigma} \cdot \mathbf{n} = \mathbf{0}$
Solid	← fluid	$\boldsymbol{\sigma} \cdot \mathbf{n} = -p_1 \mathbf{n} + ik_s \eta_0 (\mathbf{v}_{\text{sl}} - \mathbf{v}_1)$
Fluid	← solid	$\mathbf{v}_1 \cdot \mathbf{n} = \mathbf{v}_{\text{sl}} \cdot \mathbf{n} + \frac{i}{k_s} \nabla_{\parallel} \cdot (\mathbf{v}_{\text{sl}} - \mathbf{v}_1)_{\parallel}$
Fluid	← air	$p_1 = 0$

5. RESULTS AND DISCUSSION

5.1. Electrical impedance measurements

The electrical impedance spectrum $Z(f)$ of the unloaded and loaded Pz27 transducer was measured after each step in the fabrication procedure. The material parameters of the specific Pz27 transducer used in this study, were obtained by electrical impedance spectroscopy (UEIS), following the procedure described in Ref. [21], based on the measured $Z(f)$ of the unloaded transducer. The result is shown in Fig. 2(a), where it is seen that the fitted spectrum $|Z(f)|$ agrees well with the measured one. The piezoelectric parameters obtained from this UEIS fitting, were then subsequently used together with the remaining material parameters listed in Section B of the Appendix to simulate numerically the pressure field p_1 , the displacement field \mathbf{u} , and the electric potential φ of the transducer-glass-capillary-tube system. The measured and the simulated impedance spectrum of the full system in the frequency range 3.3 to 4.3 MHz are shown in Fig. 2(b), and good agreement is found. Numerical simulations were performed using both the fitted values, and the values for Pz27 given in Ref. [21]. The discrepancy between the two resulting spectra emphasizes the need of obtaining fitted material parameters for the specific transducer used in the study. The remaining deviations from the measured impedance spectrum stem from uncertainties in the glass material parameters, which were taken from literature and not fitted by UEIS.

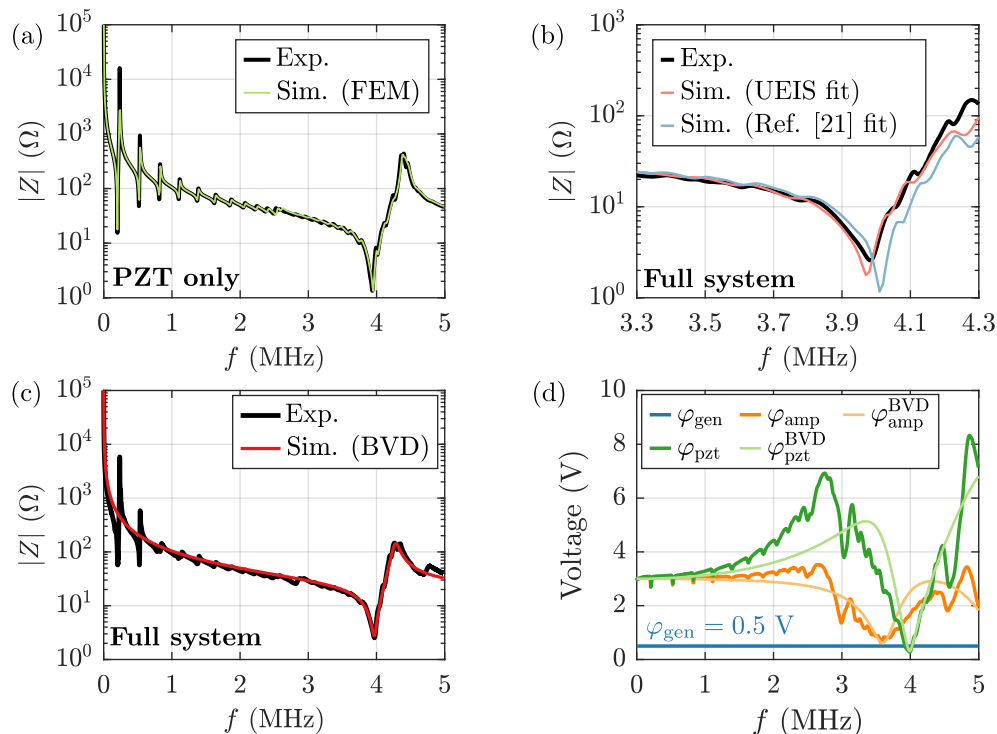


FIG. 2. (a) Measured (black) and simulated (green) electrical impedance spectrum $|Z(f)|$ in the frequency range 0.5 - 5000 kHz of the unloaded Pz27 disk. (b) Measured (black) and simulated $|Z(f)|$ for 3.3 - 4.3 MHz, using either UEIS fitted parameters (red) or the parameters from Ref. [21] (blue) of the full system consisting of Pz27 disk, glue layer and liquid-filled glass capillary tube. (c) The measured $|Z(f)|$ (black) for 0.5 - 5000 kHz of the full system (Pz27 disk, glue layer, and liquid-filled glass capillary tube), and the computed $|Z(f)|$ (red) based on the single-frequency BVD-model of Section 2.2.4. (d) The three measured voltage amplitudes versus frequency f at different points in the circuit: φ_{pzt} (dark-green) obtained by four-probe measurements directly across the piezoelectric transducer, φ_{amp} (dark-orange) measured at the output of the amplifier, φ_{gen} (dark-blue) measured at the signal generator. Also shown are the two *LTspice*-simulated voltage amplitudes: $\varphi_{\text{pzt}}^{\text{BVD}}$ (light green) and $\varphi_{\text{amp}}^{\text{BVD}}$ (light orange) computed from the BVD-model.

5.2. Impact of cable and circuit resonances on measured voltage amplitude

Using the measured impedance spectrum $Z(f)$ of the full system around the 4-MHz resonance, we obtain the required parameters to describe the transducer through the BVD model of Section 2.2.4, and we find $C_0 = 1.28$ nF, $C_1 = 207$ pF, $L_1 = 7.69$ μ H, and $R_1 = 2.59$ Ω . We estimate for each of the two wires connecting the amplifier and the transducer that $R_{\text{wire}} = 1$ Ω and $L_{\text{wire}} = 411$ nH. In Fig. 2(c), we compare $Z(f)$ computed from the BVD model with the measured $Z(f)$. It is seen that the BVD model captures well the characteristics around the 4-MHz resonance of the transducer, and it can therefore aid the understanding of the circuit characteristics.

When comparing the voltage amplitudes at various points in the circuit using a constant generator voltage amplitude $\varphi_{\text{gen}} = 0.5$ V, we find as shown in Fig. 2(d) that for most of the frequencies in the range 0.5 - 5000 kHz, the voltage amplitude φ_{pzt} across the transducer is larger than the voltage amplitude φ_{amp} right after the amplifier. This may seem counter-intuitive, but given the resonant nature of the circuit, charge may build up on the capacitive circuit elements. We furthermore find two frequencies where the voltage amplitude is minimal: At $f_{\text{amp}} = 3.56$ MHz, the impedance of the full circuit has an impedance minimum, and at $f_{\text{pzt}} = 3.98$ MHz, the impedance of the transducer has a minimum. The down-shift of f_{amp} by 0.42 MHz from f_{pzt} is due to the parasitic inductance of the wire connecting the amplifier and the transducer. We note that if the voltage amplitude is recorded right after the amplifier, and not directly across the transducer, a wrong estimate of the voltage amplitude and power dissipation of the transducer may result. Furthermore, the parasitic inductance minimizes the power transfer from the amplifier to the transducer, and therefore it is in general beneficial to minimize this inductance by use of shortened and shielded cables. To minimize the ratio $r = f_{\text{amp}}/f_{\text{pzt}}$, the inductance of the wire L_{wire} should be minimized according to

$$L_{\text{wire}} < \frac{(1 - r^2)}{2r^2} \frac{C_1 L_1}{C_1 + C_0(1 - r^2)}. \quad (16)$$

In our circuit, it is required that $L_{\text{wire}} < 70$ nH to keep the mismatch of f_{circuit} and f_{pzt} below 1 %. This is typically hard to achieve, as it requires very thin and short wires. Alternatively, a capacitor $C_{\text{comp}} = (2\pi f_{\text{comp}})^{-2} L_{\text{wire}}^{-1}$ in series with the wire could be used to counteract the impact of L_{wire} at frequency f_{comp} . Further improvements of the circuit could be obtained by impedance-matching the load impedance Z_{load} to the source impedance Z_{source} , by adding circuit components to the load such that $Z_{\text{source}} = Z_{\text{load}}^*$ [19].

5.3. Voltage and power dissipation

The voltage amplitudes and power dissipation in a frequency sweep are depending significantly on the chosen electrical excitation method in the actuation process. In Fig. 3(a)-(c) are shown frequency sweeps of the the voltage amplitudes φ_{gen} and φ_{pzt} , and the average dissipated power P_{pzt} for the three considered cases of constant φ_{gen} , constant φ_{pzt} , and constant P_{pzt} .

The first case with constant $\varphi_{\text{gen}} = 1$ V is shown in Fig. 3(a). It is seen that φ_{pzt} and P_{pzt} are minimal at or close to the transducer impedance minimum at $f_{\text{pzt}} = 3.98$ MHz. This is not an ideal situation, because many systems are designed with a resonance close to the nominal transducer resonance in mind. Instead, it is beneficial to stabilize either φ_{pzt} or P_{pzt} .

The second case with constant $\varphi_{\text{pzt}} = 0.5$ V is shown in Fig. 3(b). Both φ_{gen} and P_{pzt} have a narrow peak near $f_{\text{pzt}} = 3.98$ MHz. As will be discussed in Sections 5.5.4 and 5.5.5, this might not be ideal for particle focusing experiments when comparing device performances over wider frequency ranges.

The third case with constant $P_{\text{pzt}} = 50$ mW is shown in Fig. 3(c). To stabilize P_{pzt} , the voltage φ_{gen} needs to be adjusted according to the electrical impedance spectrum of the transducer. The voltage φ_{gen} needs to be higher when running the transducer on-resonance, compared to off-resonance. As in the first case, the voltage amplitude φ_{pzt}

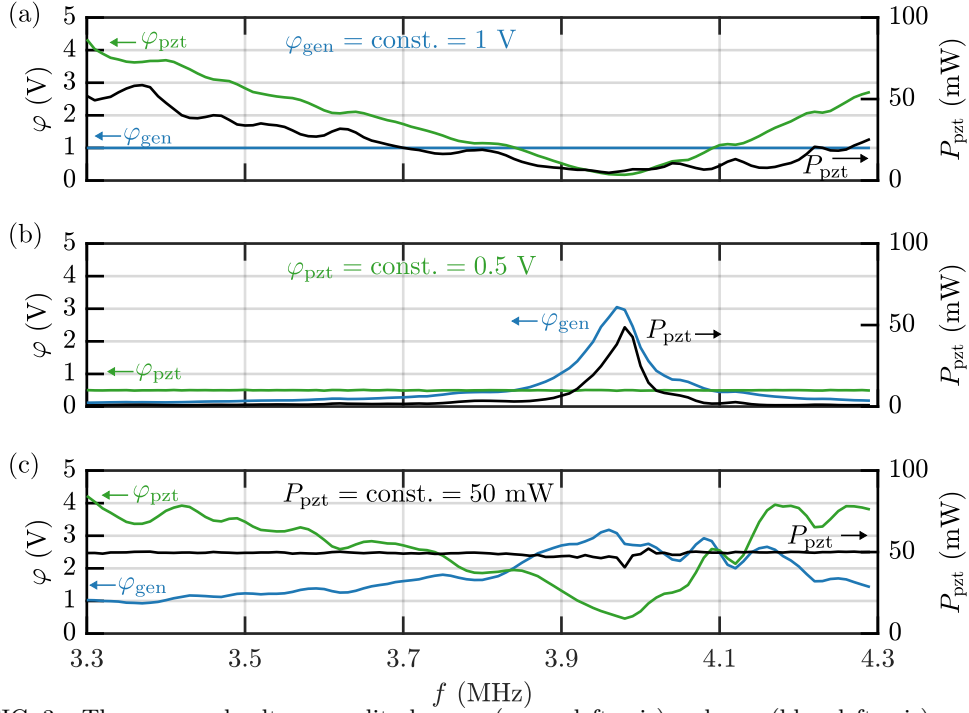


FIG. 3. The measured voltage amplitudes φ_{pzt} (green, left axis) and φ_{gen} (blue, left axis) as well as the measured average power dissipation P_{pzt} (black, right axis) plotted versus frequency for 3.3 - 4.3 MHz for the three cases (a) constant voltage φ_{gen} at the signal generator, (b) constant voltage φ_{pzt} across the piezoelectric transducer, and (c) P_{pzt} constant average power dissipation.

is minimal at the resonance $f_{\text{pzt}} = 3.98$ MHz. Other effects, such as the non-linear gain of the amplifier and non-linearity of the piezoelectric transducer, may lead to increased discrepancies between φ_{gen} and φ_{pzt} , which furthermore emphasizes the need to monitor φ_{pzt} and P_{pzt} , and to specify which of them, if any, is kept constant.

5.4. Average acoustophoretic particle speed

When the acoustic pressure field p_1 is switched on via the Pz27 transducer in our setup shown in Fig. 1, polystyrene microparticles inside the water-filled capillary tube acquire an acoustophoretic velocity v_{ps} , see Eqs. (7), (13) and (14), proportional to the acoustic radiation force \mathbf{F}^{rad} , see Eq. (6). For the above three cases, the experimental results for the average particle speed v_{exp} are shown in Fig. 4(a), and the corresponding results for P_{pzt} are shown in Fig. 4(b). In the case of constant $\varphi_{\text{gen}} = 1$ V, we observe the highest particle speed at $f = f_{\text{res}}^{\text{gen}} = 4.24$ MHz with $v_{\text{exp}} \approx 46 \mu\text{m s}^{-1}$. For constant $\varphi_{\text{pzt}} = 0.5$ V, we find the highest particle speed at $f = f_{\text{exp}}^{\varphi} = 3.98$ MHz with $v_{\text{exp}} \approx 71 \mu\text{m s}^{-1}$. Finally, for constant $P_{\text{pzt}} = 50$ mW, a resonance appears at $f = f_{\text{exp}}^{\text{P}} = 4.03$ MHz with $v_{\text{exp}} \approx 77 \mu\text{m s}^{-1}$. Furthermore, for $\varphi_{\text{pzt}} = 0.5$ V and $P_{\text{pzt}} = 50$ mW, we observe a local resonance at $f = f_{\text{width}}^{(10)} = 3.51$ MHz. This resonance relates to an acoustic mode with 5 wavelengths along the y -direction, leading to particle focusing in 10 nodal lines parallel to length and evenly distributed across the width of the microchannel above the center region of the Pz27 transducer, as discussed further in Section 5.5.5.

When analyzing the measurements in Fig. 4(b) of the power dissipation in the three cases, we find that, when driving the transducer at constant φ_{pzt} , a clear maximum in P_{pzt} appears at $f_{\text{exp}}^{\varphi} = 3.98$ MHz, but conversely, P_{pzt} has a minimum at the same frequency for constant φ_{gen} . The reason is that at this frequency, the transducer has an intrinsic

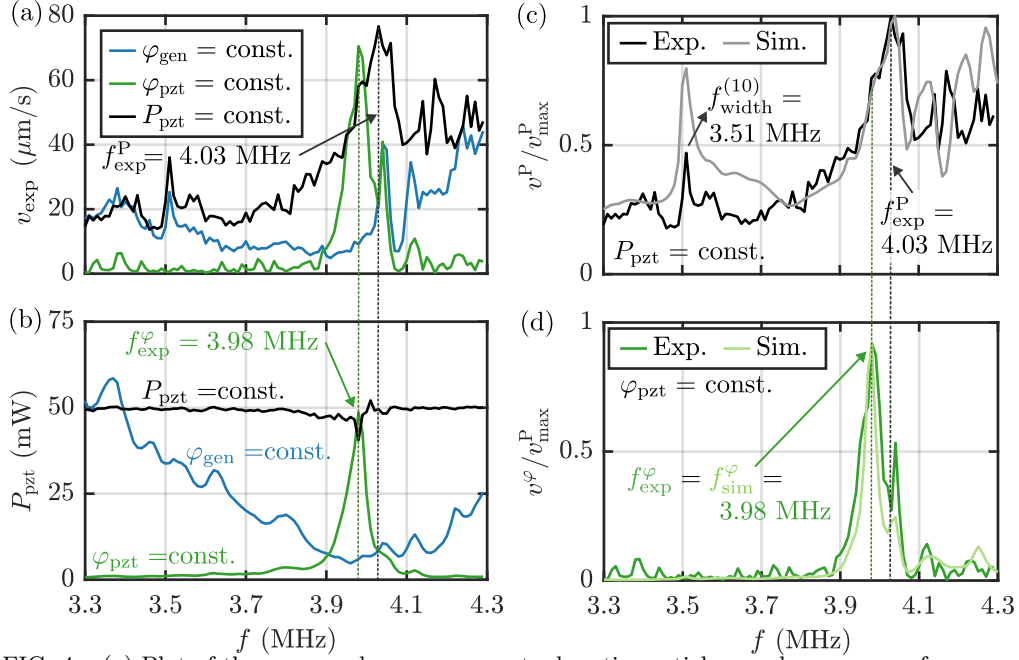


FIG. 4. (a) Plot of the measured average acoustophoretic particle speed v_{exp} versus frequency f in the range 3.3 - 4.3 MHz. (b) The measured power dissipation P_{pzt} in the transducer versus f for 3.3 - 4.3 MHz for the three cases of constant voltage φ_{gen} at the signal generator, constant voltage φ_{pzt} across the piezoelectric transducer, and constant average power dissipation P_{pzt} . (c) The experimental (black) and simulated (gray) normalized average particle speed v^P/v_{max}^P versus frequency f at constant-power dissipation $P_{\text{pzt}} = 50$ mW. (d) The experimental (dark-green) and simulated (light-green) normalized average particle speed $v^\varphi/v_{\text{max}}^\varphi$ versus frequency f at constant transducer voltage $\varphi_{\text{pzt}} = 0.5$ V.

resonance and thus a minimum in its impedance. Lastly, we note that experimentally it is difficult to perfectly stabilize P_{pzt} near the transducer resonance $f_{\text{exp}}^\varphi = 3.98$ MHz. This difficulty is likely due to on-resonance heating effects of the transducer.

5.5. Comparing numerical simulations with experiments

In Fig. 4(c) using constant $P_{\text{pzt}} = 50$ mW, the measured $v_{\text{exp}}^P/v_{\text{max}}^P$ and the simulated $v_{\text{sim}}^P/v_{\text{max}}^P$ average acoustophoretic speed, normalized by the measured maximum speed $v_{\text{max}}^P = \max|v_{\text{exp}}^P|$, are plotted versus frequency for 3.3 - 4.3 MHz. The agreement between the two curves is good, and they both show a resonance at nearly the same frequency $f = f_{\text{exp}}^P = 4.03$ MHz and $f = f_{\text{sim}}^P = 4.04$ MHz, respectively. A similar plot is shown Fig. 4(d), but now for the case of constant $\varphi_{\text{pzt}} = 0.5$ V, namely the measured $v_{\text{exp}}^\varphi/v_{\text{max}}^\varphi$ and the simulated $v_{\text{sim}}^\varphi/v_{\text{max}}^\varphi$ versus frequency with the same normalization v_{max}^φ as before. Again, the agreement between simulation and experiment is good, and both curves have a maximum at $f = f_{\text{exp}}^\varphi = f_{\text{sim}}^\varphi = 3.98$ MHz, about 50 kHz lower than the constant-power resonance frequency $f_{\text{exp}}^P = 4.03$ MHz.

Some interesting features are seen in the measured and simulated spectrum of the constant-voltage acoustophoretic velocity spectrum $v_{\text{exp}}^\varphi(f)$ in Fig. 4(d). Its maximum, obtained at $f_{\text{exp}}^\varphi = 3.98$ MHz, is 8% less than the one obtained in the constant-power velocity spectrum $v^P(f)$ in Fig. 4(c), $v_{\text{max}}^\varphi = 0.92 v_{\text{max}}^P$. Moreover, far from being at the maximum, $v_{\text{exp}}^\varphi(f_{\text{exp}}^P) = 0.27 v_{\text{max}}^P$ is a local minimum. Clearly, the optimal operating condition for acoustophoresis is to run the system at f_{exp}^P with constant-power actuation. Operating directly at the transducer resonance at $f_{\text{exp}}^\varphi = 3.98$ MHz, is not equally efficient

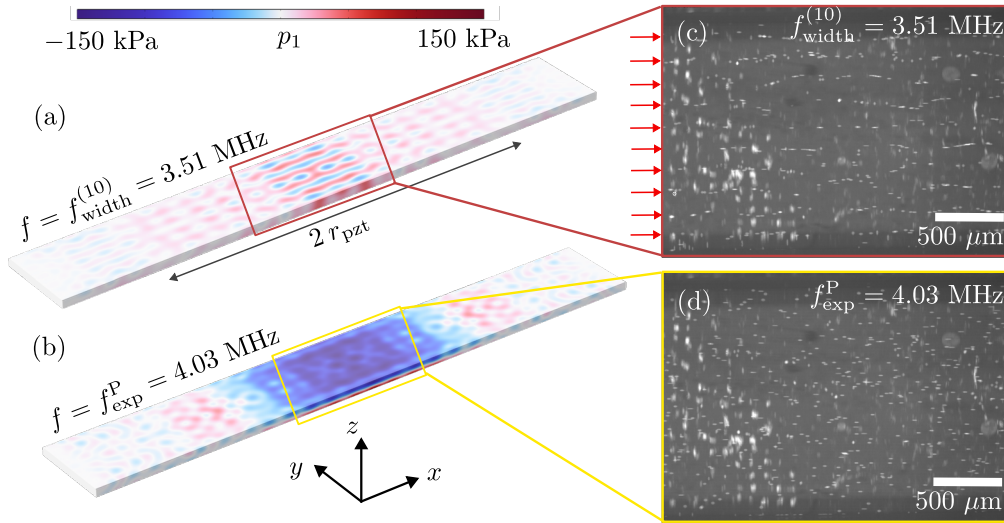


FIG. 5. Color plot from -150 kPa (blue) to 150 kPa (red) of the simulated acoustic pressure field p_1 inside the fluid channel at (a) $f = f_{\text{width}}^{(10)} = 3.51$ MHz with a standing-5-wavelength resonance mode in the y -direction (10 nodal lines above the center region of the transducer), and (b) at $f = f_{\text{exp}}^P = 4.03$ MHz with a standing- $\frac{1}{2}$ -wavelength resonance mode in z -direction. (c) Micrograph of the particles focused in 10 nodal lines (marked by red arrows) inside the microfluidic channel after 4 s at the resonance frequency $f_{\text{width}}^{(10)} = 3.51$ MHz. (d) Micrograph of the particles focused in 1 nodal plane (the xy -plane) inside the microfluidic channel after 4 s at the resonance frequency $f_{\text{exp}}^P = 4.03$ MHz.

due to the low impedance of the transducer and the resulting high power dissipation at this frequency. Constant-voltage frequency sweeps can be misleading in that regard.

In the simulation and experiment with constant P_{pzt} , see Fig. 4(a, c), a local maximum in the average particle speed v is observed at $f = f_{\text{width}}^{(10)} = 3.51$ MHz. In Fig. 5(a,b), we compare the simulated pressure field at this frequency with the simulation results at $f = f_{\text{exp}}^P = 4.03$ MHz. Images of the particles after 4 s at the two corresponding frequencies are shown in Fig. 5(c) and (d). Both in the numerically simulated pressure field, as well as in the measured particle positions, we observe in the x - y plane at $f = f_{\text{width}}^{(10)} = 3.51$ MHz, the formation of 10 nodal lines parallel to the tube axis along the x direction, and with an equidistant distribution across the width, see Fig. 5(c). In contrast, at the main resonance at $f_{\text{exp}}^P = 4.03$ MHz shown in Fig. 5(d), we observe particle focusing in the x - y center plane of the glass capillary tube, above the center region of the Pz27 transducer, caused by the standing half-wave in the vertical z -direction. No transverse nodal lines are observed here.

6. CONCLUSION

Monitoring power dissipation in and voltage across the piezoelectric transducer is important and helpful for understanding and optimizing the performance of acoustofluidic systems. As shown by our measurements on the setup shown in Fig. 1, the voltage can differ significantly between amplifier output and transducer, due to the varying impedance of the transducer at different frequencies. In this work, we compared the performance of an acoustofluidic device using three types of actuation: (Case 1) Supplying a constant voltage amplitude φ_{gen} to the amplifier input from the signal generator, (Case 2) driving the piezoelectric transducer using constant-voltage actuation φ_{pzt} , and (Case 3) keeping the power dissipation P_{pzt} in the transducer constant. The acoustofluidic performance was evaluated in terms of the average acoustophoretic particle speed v in the microfluidic channel measured with 3D particle tracking velocimetry and computed numerically, see Fig. 4.

Case 1, performing frequency sweeps with constant φ_{gen} , which is typically used for acoustofluidic devices, may result in a misleading identification of the ideal actuation frequency. The reason is that the power dissipation in the transducer is dependent of the impedance of the transducer as well as the resonant behavior of the cables connecting amplifier and transducer. Instead, keeping a constant power P_{pzt} is a better choice for obtaining a reproducible characterization of the intrinsic properties of acoustofluidic devices.

Case 2, frequency sweeps with constant φ_{pzt} often result in high power dissipation at the transducer resonance frequency f_{exp}^{φ} , where the impedance of the transducer is at a minimum. Therefore, the strongest acoustofluidic response will be observed closest to this frequency, but it is likely not the most power-efficient frequency, as it results in increased heating and comes at the cost of high input powers. Acoustofluidic applications, however, are often constrained by power-limitations of the frequency generator or the amplifier, as well as the requirement of maintaining a defined temperature to enable the processing of biological samples.

Case 3, frequency sweeps with constant P_{pzt} appear to be a better measure to compare device performance across frequencies, as this compensates for the decrease in impedance at the transducer resonance. As a consequence, also finer details in the acoustic fields that occur at frequencies further away from the transducer resonance frequency can be observed. This is exemplified by the transverse resonance in the width direction at $f = f_{\text{width}}^{(10)} = 3.51$ MHz, see Fig. 5(a) and (c); a resonance clearly visible as a strong peak in the constant-power spectrum in Fig. 4(c), but not visible in the constant-voltage spectrum in Fig. 4(d). Keeping P_{pzt} constant, enhances the intrinsic properties of the device performance, as it does not depend on the wiring. In conclusion, frequency sweeps with constant power may help to identify the most power-efficient actuation frequencies leading to the desired acoustofluidic response, and it allows a more clear-cut comparison of different acoustofluidic resonances across the frequency spectrum.

Lastly, the external circuitry, see Fig. 1, may have an impact on the resonance behavior of the setup. In this work, the parasitic impact of the wire inductance, connecting the amplifier and the transducer, was observed. We note that by fine-tuning the impedance of the external circuitry to match the impedance of the transducer at resonance, the power transfer to the transducer can be increased. Such an impedance matching is common in many other fields. Considering the whole circuit, rather than just the piezoelectric transducer in an acoustofluidic setup, therefore can be beneficial to further improve system performance in various acoustofluidic applications.

ACKNOWLEDGEMENTS

Author contributions: Conceptualization, F.L., H.B., and M.R.; methodology, F.L., H.B., and M.R.; software, F.L. and M.R.; validation, F.L., H.B., and M.R.; formal analysis, F.L., H.B., and M.R.; investigation, F.L., H.B., and M.R.; resources, F.L. and M.R.; data curation, F.L.; concluding discussions, F.L., H.B., and M.R.; writing—original draft preparation, F.L.; writing—review and editing, F.L., H.B. and M.R.; visualization, F.L., H.B., and M.R.; supervision: H.B. on theory and simulation, M.R. on experiment; project administration, H.B. and M.R.; funding acquisition, H.B. and M.R. All authors have read and agreed to the published version of the manuscript.

Funding: This work is part of the Eureka Eurostars-2 joint programme E!113461 AcouPlast project funded by Innovation Fund Denmark, grant no. 9046-00127B, and Vinnova, Sweden’s Innovation Agency, grant no. 2019-04500, with co-funding from the European Union Horizon 2020 Research and Innovation Programme. MR acknowledges the financial support by the VILLUM foundation, grant no. 00036098.

Data availability statement: The data presented in this study are available on request from the corresponding author.

Conflicts of interest: The authors declare no conflict of interest. The funders had no role in the design of the study; in the collection, analyses, or interpretation of data; in the writing of the manuscript; or in the decision to publish the results.

Abbreviations

The following abbreviations are used in this manuscript:

BVD	Butterworth–Van Dyke
GDPT	General Defocusing Particle Tracking
PML	Perfectly Matched Layer
UEIS	Ultrasound Electrical Impedance Spectroscopy

Appendix A: Convergence analysis for the mesh and perfectly matched layer

To confirm that the meshing of our finite element model is sufficient we perform mesh convergence testing, following Ref. [26]. We compute the convergence of a given field f compared to a reference solution f_{ref} which is obtained at a high mesh resolution, by gradually increasing the mesh resolution with scale s and computing the L_2 -norm,

$$C[f(s)] = \sqrt{\frac{\int_{\Omega} |f(s) - f_{\text{ref}}|^2 dV}{\int_{\Omega} |f_{\text{ref}}|^2 dV}}. \quad (\text{A1})$$

The results are shown in Fig. 6. For our final mesh we use a mesh scale of $s = 8$ and find a convergence of 3.8% for the displacement u_x , 2.7% for the displacement u_y , 1.9% for the displacement u_z , 1.5% for the pressure field p_1 , and 0.8% for the electric potential φ . The length of the perfectly matched layer (PML) region is chosen relative to the longitudinal wavelength in glass $\lambda_{\text{lo}}^{\text{glass}}$. In our convergence study it was gradually increased from $0.1\lambda_{\text{lo}}^{\text{glass}}$ to $2\lambda_{\text{lo}}^{\text{glass}}$. We find good convergence starting from $L_{\text{pml}} = 0.7\lambda_{\text{lo}}^{\text{glass}} \approx 921 \mu\text{m}$ with convergence below 1% compared to the longest simulated PML layer.

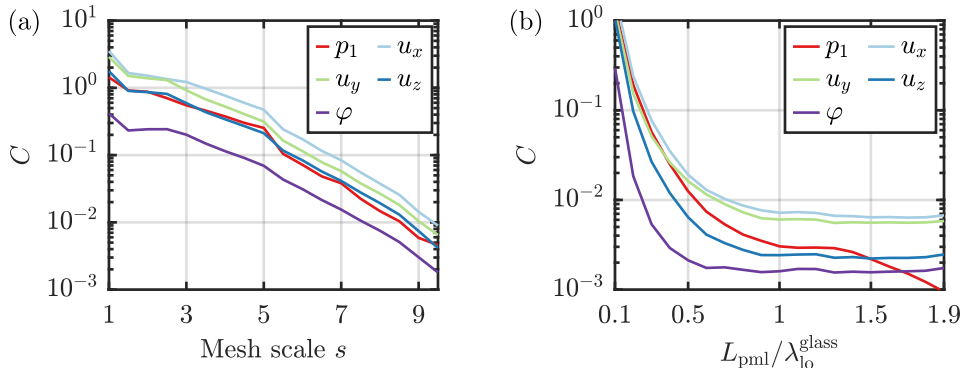


FIG. 6. (a) Convergence of the pressure field p_1 , displacement field components u_x , u_y , u_z and the electric potential φ with increasing mesh scale s . (b) Convergence of the pressure field p_1 , displacement field components u_x , u_y , u_z with increasing length of the PML layer L_{pml} , expressed relative to the wavelength in glass $\lambda_{\text{lo}}^{\text{glass}}$.

Appendix B: Material parameters

We study 10 μm -diameter polystyrene particles suspended in a liquid at a temperature of $T = 24 \text{ }^\circ\text{C}$ to match the laboratory conditions. To obtain neutral buoyancy of the particles, distilled water is mixed with the chemical OptiPrep, resulting in a volume fraction of 17% (v/v) OptiPrep in water. The glass capillary tube is made from borosilicate glass, the transducer is PZT, and the glue layer is the urethane-related resin NOA86H. The values of the material parameters for the liquid, polystyrene particles and glass capillary tube are taken from the literature. The material parameters for the glue layer and the piezoelectric transducer were obtained via ultrasound electrical impedance spectroscopy, as described in [21]. The material parameters used in the numerical simulations are summarized in Table 2.

TABLE 2. List of parameters at 24 °C used in the numerical simulation: the aqueous OptiPrep solution, 10 μm -diameter polystyrene particles, borosilicate glass, glue, and PZT. For PMMA $C_{12} = C_{11} - 2C_{44}$. For PZT $C_{12} = C_{11} - 2C_{66}$.

Parameter	Symbol	Value	Unit
<i>0.83/0.17 (v/v) water-OptiPrep solution</i> [27, 28]			
Mass density	ρ_0	1054	kg m^{-3}
Speed of sound	c_0	1501	m s^{-1}
Compressibility	κ_0	421	TPa^{-1}
Dynamic viscosity	η_0	0.911	mPa s
Bulk viscosity	η_0^b	2.551	mPa s
<i>Polystyrene</i> [29]			
Mass density	ρ_{ps}	1052	kg m^{-3}
Compressibility	κ_{ps}	238	TPa^{-1}
Monopole coefficient	f_0	0.434	
Dipole coefficient	f_1	0	
<i>Borosilicate glass</i> [30, 31]			
Mass density	ρ_{sl}	2230	kg m^{-3}
Elastic modulus	C_{11}	64.84 – i0.03	GPa
Elastic modulus	C_{44}	24.32 – i0.01	GPa
<i>Glue (NOA86H)</i> (measured using UEIS-method [21])			
Mass density	ρ_{sl}	1250	kg m^{-3}
Elastic modulus	C_{11}	4.65 – i0.51	GPa
Elastic modulus	C_{44}	1.21 – i0.12	GPa
<i>PZT (Pz27)</i> (measured using UEIS-method [21])			
Mass density	ρ_{sl}	7707	kg m^{-3}
Elastic modulus	C_{11}	121 – i0.67	GPa
Elastic modulus	C_{12}	72.4 + i0.61	GPa
Elastic modulus	C_{13}	75.6 + i0.12	GPa
Elastic modulus	C_{33}	116 – i0.54	GPa
Elastic modulus	C_{44}	21.4 – i0.83	GPa
Coupling constant	e_{15}	13.4	C m^{-2}
Coupling constant	e_{31}	–5.2	C m^{-2}
Coupling constant	e_{33}	16.1	C m^{-2}
Electric permittivity	ϵ_{11}	925 ϵ_0	
Electric permittivity	ϵ_{33}	791 ϵ_0	

- [1] R. Barnkob, P. Augustsson, T. Laurell, and H. Bruus, Measuring the local pressure amplitude in microchannel acoustophoresis, [Lab Chip](#) **10**, 563 (2010).
- [2] R. Barnkob, I. Iranmanesh, M. Wiklund, and H. Bruus, Measuring acoustic energy density in microchannel acoustophoresis using a simple and rapid light-intensity method, [Lab Chip](#) **12**, 2337 (2012).
- [3] F. Lickert, M. Ohlin, H. Bruus, and P. Ohlsson, Acoustophoresis in polymer-based microfluidic devices: Modeling and experimental validation, [J. Acoust. Soc. Am.](#) **149**, 4281 (2021).
- [4] A. Barani, P. Mosaddegh, S. Haghjooy Javanmard, S. Sepehrirahnama, and A. Sanati-Nezhad, Numerical and experimental analysis of a hybrid material acoustophoretic device for manipulation of microparticles, [Sci. Rep.](#) **11**, 1 (2021).
- [5] W. Qiu, T. Baasch, and T. Laurell, Enhancement of acoustic energy density in bulk-wave-acoustophoresis devices using side actuation, [Phys. Rev. Appl.](#) **17**, 044043 (2022).
- [6] R. Dubay, C. Lissandrello, P. Swierk, N. Moore, D. Doty, and J. Fiering, Scalable high-throughput acoustophoresis in arrayed plastic microchannels, [Biomicrofluidics](#) **13**, 034105 (2019).
- [7] C. Lissandrello, R. Dubay, K. T. Kotz, and J. Fiering, Purification of lymphocytes by acoustic separation in plastic microchannels, [SLAS Technology](#) **23**, 352 (2018).

- [8] M. G. Kim, S. Yoon, H. H. Kim, and K. K. Shung, Impedance matching network for high frequency ultrasonic transducer for cellular applications, *Ultrasonics* **65**, 258 (2016).
- [9] M. Garcia-Rodriguez, J. Garcia-Alvarez, Y. Yañez, M. Garcia-Hernandez, J. Salazar, A. Turo, and J. Chavez, Low cost matching network for ultrasonic transducers, *Phys. Procedia* **3**, 1025 (2010).
- [10] J. S. Emeterio, A. Ramos, P. Sanz, and A. Ruiz, Evaluation of impedance matching schemes for pulse-echo ultrasonic piezoelectric transducers, *Ferroelectrics* **273**, 297 (2002).
- [11] I. Leibacher, S. Schatzer, and J. Dual, Impedance matched channel walls in acoustofluidic systems, *Lab Chip* **14**, 463 (2014).
- [12] P. Ohlsson, K. Petersson, P. Augustsson, and T. Laurell, Acoustic impedance matched buffers enable separation of bacteria from blood cells at high cell concentrations, *Sci. Rep.* **8**, 2045 (2018).
- [13] A. Huang, W. Connacher, M. Stambaugh, N. Zhang, S. Zhang, J. Mei, A. Jain, S. Alluri, V. Leung, A. E. Rajapaksa, *et al.*, Practical microcircuits for handheld acoustofluidics, *Lab Chip* **21**, 1352 (2021).
- [14] N. R. Skov, J. S. Bach, B. G. Winkelmann, and H. Bruus, 3D modeling of acoustofluidics in a liquid-filled cavity including streaming, viscous boundary layers, surrounding solids, and a piezoelectric transducer, *AIMS Mathematics* **4**, 99 (2019).
- [15] N. R. Skov, P. Sehgal, B. J. Kirby, and H. Bruus, Three-dimensional numerical modeling of surface-acoustic-wave devices: Acoustophoresis of micro- and nanoparticles including streaming, *Phys. Rev. Applied* **12**, 044028 (2019).
- [16] A. G. Steckel and H. Bruus, Numerical study of bulk acoustofluidic devices driven by thin-film transducers and whole-system resonance modes, *J. Acoust. Soc. Am.* **150**, 634 (2021).
- [17] J. S. Bach and H. Bruus, Theory of pressure acoustics with viscous boundary layers and streaming in curved elastic cavities, *J. Acoust. Soc. Am.* **144**, 766 (2018).
- [18] M. Settnes and H. Bruus, Forces acting on a small particle in an acoustical field in a viscous fluid, *Phys. Rev. E* **85**, 016327 (2012).
- [19] V. T. Rathod, A review of electric impedance matching techniques for piezoelectric sensors, actuators and transducers, *Electronics* **8**, 169 (2019).
- [20] H. Huang and D. Paramo, Broadband electrical impedance matching for piezoelectric ultrasound transducers, *IEEE Trans. Ultrason. Ferroelectr. Freq. Control* **58**, 2699 (2011).
- [21] W. N. Bodé, F. Lickert, P. Augustsson, and H. Bruus, Determination of the complex-valued elastic moduli of polymers by electrical impedance spectroscopy for ultrasound applications, *Phys. Rev. Applied* **submitted**, 10 pages (2022), <https://arxiv.org/abs/2204.06464>.
- [22] R. Barnkob, C. J. Kähler, and M. Rossi, General defocusing particle tracking, *Lab Chip* **15**, 3556 (2015).
- [23] M. Rossi and R. Barnkob, A fast and robust algorithm for general defocusing particle tracking, *Meas. Sci. Technol.* **32**, 014001 (2020).
- [24] R. Barnkob and M. Rossi, Defocustracker: A modular toolbox for defocusing-based, single-camera, 3d particle tracking, *Journal of Open Research Software* **9**, 22 (2021).
- [25] W. N. Bodé and H. Bruus, Numerical study of the coupling layer between transducer and chip in acoustofluidic devices, *J. Acoust. Soc. Am.* **149**, 3096 (2021).
- [26] P. B. Muller, R. Barnkob, M. J. H. Jensen, and H. Bruus, A numerical study of microparticle acoustophoresis driven by acoustic radiation forces and streaming-induced drag forces, *Lab Chip* **12**, 4617 (2012).
- [27] P. B. Muller and H. Bruus, Numerical study of thermoviscous effects in ultrasound-induced acoustic streaming in microchannels, *Phys. Rev. E* **90**, 043016 (2014).
- [28] J. T. Karlsen, P. Augustsson, and H. Bruus, Acoustic force density acting on inhomogeneous fluids in acoustic fields, *Phys. Rev. Lett.* **117**, 114504 (2016).
- [29] J. T. Karlsen and H. Bruus, Forces acting on a small particle in an acoustical field in a thermoviscous fluid, *Phys. Rev. E* **92**, 043010 (2015).
- [30] *Borosilicate glass substrates*, SCHOTT, SCHOTT Suisse SA, 2 Rue Galilée, Yverdon, Switzerland, https://www.epfl.ch/research/facilities/cmi/wp-content/uploads/2020/05/D263T_d.pdf, accessed 18 August 2022.
- [31] A. G. Steckel, H. Bruus, P. Muralt, and R. Matloub, Fabrication, characterization, and simulation of glass devices with AlN thin-film transducers for excitation of ultrasound resonances, *Phys. Rev. Applied* **16**, 014014, 1 (2021).